Available online at www.sciencedirect.com
SCIENCE DIRECT®
International Journal of Heat and Mass Transfer 48 (2005) 1403–1412
International Journal of HEAT and MASS TRANSFER
www.elsevier.com/locate/ijhmt

Pressure variation in a natural circulation loop with end heat exchangers

N.M. Rao [a,*], B. Maiti [b], P.K. Das [b]

[a] Department of Mechanical Engineering, Dr. Babasaheb Ambedkar Technological University, 'Vidyavihar', Lonere 402 103, Maharashtra, India
[b] Department of Mechanical Engineering, Indian Institute of Technology, Kharagpur 721 302, West Bengal, India

Received 25 September 2003
Available online 25 January 2005

Abstract

The pressure variation in a natural circulation loop has been investigated for both steady state and transient operating conditions. The loop exchanges heat with hot and cold external fluid streams through counterflow concentric tube heat exchangers. Considering spatial changes only in the direction of the loop length, closed form expressions have been obtained for pressure difference under steady state condition. An iterative scheme based on finite element method (FEM) has been formulated to solve the conservation equations in the transient state. The variation of dynamic pressure and its relationship with the variation of temperature field and circulation rate has been described.

Keywords: Total pressure; Dynamic pressure; Natural circulation loop; Heat exchangers; FEM

1. Introduction

Natural circulation loops (NCLs) are used in diverse engineering applications due to their simple construction and highly reliable operation. Their application ranges from the primary heat transfer loop of nuclear reactors to solar thermal systems. Thermal management of electronic packages using NCL is becoming promising day by day. However, the circulation rate and hence the cooling capacity of a NCL is not known a priori and is an implicit function of the loop geometry and the operating variables. Over the decades considerable research efforts have been spent to analyze the steady state and dynamic behavior of NCLs. Review of earlier investigations on NCL can be found in Zvirin [1], Metrol and Greif [2] and Greif [3]. Further, some interesting studies have been made on the steady state performance of NCL having figure of eight configuration [4], scaling criteria [5] and stability of toroidal loop with a variation of angle of tilt [6].

In all the above studies heat transfer zones of the NCL were simulated either considering a constant wall temperature or imposing a constant wall heat flux. However, in many applications the fluid circulating in the NCL exchanges heat with external hot and cold streams through heat exchangers. Rao et al. [7] and Rao [8] studied the steady state and transient performance of a rectangular NCL with end heat exchangers. Though they have studied the development of flow and temperature field, the variation of pressure has not been investigated either in steady state or under dynamic condition. In an

* Corresponding author. Tel.: +91 2140 275228; fax: +91 2140 275040.
E-mail address: nmuralidhararao@yahoo.com (N.M. Rao).

0017-9310/$ - see front matter © 2004 Published by Elsevier Ltd.
doi:10.1016/j.ijheatmasstransfer.2004.10.010

Nomenclature

A_s	cross sectional area, m^2
c	specific heat, kJ/kg K
C	heat capacity rate, kW/K
C^*	non-dimensional heat capacity rate, $\left(\frac{C}{(\mu cD)_{cf}}\right)$
C_f	friction factor, dimensionless
D	loop diameter, m
g	gravitational acceleration, m/s^2
Gr_L	loop Grashof number, dimensionless, $\left(\frac{\rho_{ci}^2 g\beta D^3(T_{hi}-T_{ci})}{\mu_{cf}^2}\right)$
L_1	horizontal length of the loop, m
L_2	vertical length of the loop, m
Ntu_c	$(UA)_c/C_{min,c}$ (CEHE), dimensionless
Ntu_h	$(UA)_h/C_{min,h}$ (HEHE), dimensionless
Ntu_c^*	$(UA)_c^*/C_c^*$
Ntu_h^*	$(UA)_h^*/C_h^*$
P	pressure, kN/m^2
P_S^*	non-dimensional static pressure, $\left(-\frac{\rho_{ci}^2(A_s^2)_{cf}gL_1}{\mu_{cf}^2D^2}\sin\phi S\right)$
P_t^*	non-dimensional total pressure, $\left(\frac{P_t\rho_{ci}(A_s^2)_{cf}}{\mu_{cf}^2D^2}\right)$
$\Delta P^*(S,\tau)$	non-dimensional pressure difference, $(P^*(S,\tau)-P^*(0,\tau))$
Re	Reynolds number, $\left(\frac{\rho uD}{\mu}\right)_{cf}$
s	space coordinate, m
S	non-dimensional space coordinate, $\left(\frac{s}{L_1}\right)$
t	time, s
T	temperature, K
u	velocity, m/s
UA	product of over-all heat transfer coefficient and heat transfer area, kW/K
$(UA)^*$	non-dimensional product of over-all heat transfer coefficient and heat transfer area, $\left(\frac{(UA)}{(\mu cD)_{cf}}\right)$

Greek symbols

β	thermal expansion coefficient, K^{-1}
ε	effectiveness, dimensionless, $\left(\frac{1-e^{-Ntu^*\left(1-\frac{C_{cf}^*}{C^*}\right)}}{1-\frac{C_{cf}^*}{C^*}e^{-Ntu^*\left(1-\frac{C_{cf}^*}{C^*}\right)}}\right)$
θ	non-dimensional temperature, $\left(\frac{(T-T_{ci})}{(T_{hi}-T_{ci})}\right)$
μ	viscosity, kg/m s
ρ	density, kg/m^3
τ	non-dimensional time, dimensionless, $\left(t\left[\left(\frac{\mu D}{\rho A_s}\right)_{cf}\frac{1}{L_1}\right]\right)$
ϕ	angle of inclination

Subscripts

c	cold stream
cf	coupling fluid
cfss	steady state (coupling fluid)
cfss1	steady state (downcomer)
cfss2	steady state (riser)
ci	cold stream inlet
d	dynamic
dss	steady state dynamic
dss max	maximum steady state dynamic
h	hot stream
hi	hot stream inlet
s	static
t	total
max,c	larger heat capacity rate of the fluid in CEHE side, kW/K
max,h	larger heat capacity rate of the fluid in HEHE side, kW/K
min,c	smaller heat capacity rate of the fluid in CEHE side, kW/K
min,h	smaller heat capacity rate of the fluid in HEHE side, kW/K

NCL, the conversion between static and dynamic pressure and an interaction between buoyancy head and frictional pressure drop is quite interesting. A study of the variation of pressure in the NCL helps to understand the development of flow, which is responsible for the development of the temperature field in an implicit manner. The only study in this direction is due to Mertol et al. [9], who analyzed the pressure variation in a toroidal loop with the lower half heated under constant heat flux condition and upper half cooled at a constant wall temperature.

In the present study, the steady state and transient pressure variation in a closed rectangular natural circulation loop (NCL) with end heat exchangers have been investigated. The loop MNOP, of uniform circular cross section, is placed in a vertical plane as shown in Fig. 1. Two concentric tube heat exchangers are incorporated at the lower and upper horizontal sections of the loop. The fluid inside the NCL passes through the central passage of the heat exchangers. The hot and the cold streams passes through the peripheral passages of the hot end heat exchanger (HEHE) and cold end heat exchanger (CEHE), respectively as shown in Fig. 1. Therefore, the present arrangement also represents a fluid coupled indirect heat exchanger where the circulation of the coupling fluid is caused not by any mechanical prime mover, but solely by the buoyancy force.

In this study, emphasis has been given on the critical analysis of different competing effects such as buoyancy force and viscous force; dynamic pressure and static

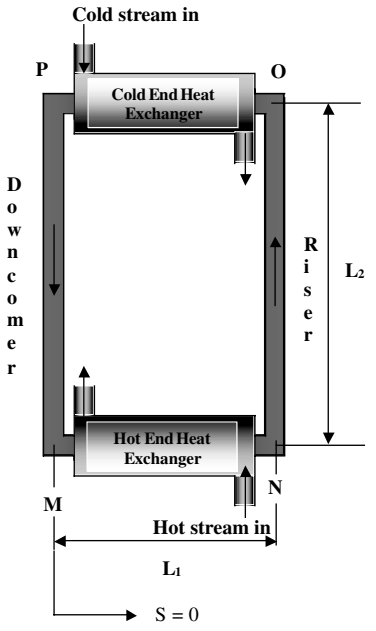

Fig. 1. Schematic diagram of a single phase NCL with end heat exchangers.

pressure. Therefore, it gives a better insight into the operation of the loop.

2. Mathematical formulation

The analysis of the rectangular NCL has been made based on the following assumptions:

- The flow is fully mixed so the velocity and temperature variation at any cross section is neglected.
- All the fluid streams are in single phase.
- Coupling fluid flows in the counter-clockwise direction and both the heat exchangers are counter current heat exchangers.
- The hot and cold stream heat capacity rates remain constant and finite.
- The over-all heat transfer coefficients and the surface area per unit length of the heat exchangers are constant throughout their length.
- The density variation in the coupling fluid has been considered only in the body force term (Boussinesq approximation).
- Riser and downcomer are adiabatic.
- Viscous dissipation and axial conduction in fluid is neglected.
- Minor losses due to bends and fittings have been neglected.

As the velocity depends only on time, the continuity equation may be written as

$$u_{\mathrm{cf}} = u_{\mathrm{cf}}(t). \tag{1}$$

The momentum equation for a differential fluid element inside the loop can be written as

$$\frac{\partial P_{\mathrm{t}}}{\partial s} = -\left[\rho_{\mathrm{cf}}\frac{\partial u_{\mathrm{cf}}}{\partial t} + \rho_{\mathrm{cf}} g\sin\phi + \frac{2C_{\mathrm{f}}\rho_{\mathrm{cf}}u_{\mathrm{cf}}^2}{D}\right]. \tag{2}$$

One can now introduce a functional relationship between friction factor, C_{f}, and Reynolds number, Re, in the following form:

$$C_{\mathrm{f}} = aRe^{-b}, \tag{3}$$

where 'a' and 'b' are constants. Relationship of this form is valid over a wide range of Reynolds number covering both laminar and turbulent region. However, the constants have different values for these two regions.

Incorporating the relationship for friction factor in the differential momentum equation, one gets,

$$\frac{\partial P_{\mathrm{t}}}{\partial s} = -\left[\rho_{\mathrm{cf}}\frac{\partial u_{\mathrm{cf}}}{\partial t} + \rho_{\mathrm{cf}} g\sin\phi + \frac{2a\mu_{\mathrm{cf}}^b\rho_{\mathrm{cf}}^{1-b}}{D^{1+b}}u_{\mathrm{cf}}^{2-b}\right]. \tag{4}$$

The density variation in the body force term may be assumed a linear function of temperature [10–12].

$$\rho_{\mathrm{cf}} = \rho_{\mathrm{ci}}[1-\beta(T_{\mathrm{cf}} - T_{\mathrm{ci}})]. \tag{5}$$

In the present work, the reference temperature has been considered as the cold stream inlet temperature.

Integrating Eq. (4) around the loop one gets the momentum equation in an integral form.

$$\frac{2(L_1+L_2)}{(A_{\mathrm{s}}c)_{\mathrm{cf}}}\frac{\partial C_{\mathrm{cf}}}{\partial t} + \frac{4a\mu_{\mathrm{cf}}^b(L_1+L_2)}{\rho_{\mathrm{cf}}(A_{\mathrm{s}}c)_{\mathrm{cf}}^{2-b}D^{1+b}}C_{\mathrm{cf}}^{2-b} + \rho_{\mathrm{ci}}g\beta\left[\int_{(2L_1+L_2)}^{2(L_1+L_2)} T_{\mathrm{cf}}\,\mathrm{d}s - \int_{L_1}^{(L_1+L_2)} T_{\mathrm{cf}}\,\mathrm{d}s\right] = 0. \tag{6}$$

Further, the variation of temperature in the fluid streams along the loop can be obtained considering the heat transfer between the streams by convection.

3. Hot end heat exchanger (HEHE)

For $0 \leqslant s \leqslant L_1$ (i.e., $s = 0$ at M, and $s = L_1$ at N), one gets the expressions for the temperature change for hot stream and coupling fluid as,

$$\frac{\partial T_{\mathrm{h}}}{\partial t} - u_{\mathrm{h}}\frac{\partial T_{\mathrm{h}}}{\partial s} + \frac{(UA)_{\mathrm{h}}}{(\rho A_{\mathrm{s}}c)_{\mathrm{h}}L_1}(T_{\mathrm{h}} - T_{\mathrm{cf}}) = 0 \tag{7}$$

and

$$\frac{\partial T_{\mathrm{cf}}}{\partial t} + u_{\mathrm{cf}}\frac{\partial T_{\mathrm{cf}}}{\partial s} + \frac{(UA)_{\mathrm{h}}}{(\rho A_{\mathrm{s}}c)_{\mathrm{cf}}L_1}(T_{\mathrm{cf}} - T_{\mathrm{h}}) = 0. \tag{8}$$

4. Cold end heat exchanger (CEHE)

For $(L_1 + L_2) \leqslant s \leqslant (2L_1 + L_2)$ (i.e., $s = (L_1 + L_2)$ at O, and $s = (2L_1 + L_2)$ at P), one can express the temperature change in the cold stream and the coupling fluid in the following form:

$$\frac{\partial T_c}{\partial t} - u_c \frac{\partial T_c}{\partial s} + \frac{(UA)_c}{(\rho A_s c)_c L_1}(T_c - T_{cf}) = 0 \tag{9}$$

while,

$$\frac{\partial T_{cf}}{\partial t} + u_{cf} \frac{\partial T_{cf}}{\partial s} + \frac{(UA)_c}{(\rho A_s c)_{cf} L_1}(T_{cf} - T_c) = 0 \tag{10}$$

5. Riser and downcomer

On the other hand, there is no heat transfer in the riser and the downcomer. Therefore, for $L_1 \leqslant s \leqslant (L_1 + L_2)$ (i.e., $s = L_1$ at N, and $s = (L_1 + L_2)$ at O), and, $(2L_1 + L_2) \leqslant s \leqslant 2(L_1 + L_2)$ (i.e., $s = (2L_1 + L_2)$ at P, and $s = 2(L_1 + L_2)$ at M),

$$\frac{\partial T_{cf}}{\partial t} + u_{cf} \frac{\partial T_{cf}}{\partial s} = 0. \tag{11}$$

The boundary conditions are

$$T_h(s,t) = T_{hi} \quad \text{at } s = L_1 \quad \text{i.e., at a station '}N\text{'}, \tag{12a}$$

$$T_c(s,t) = T_{ci} \quad \text{at } s = (2L_1 + L_2) \quad \text{i.e., at a station '}P\text{'}. \tag{12b}$$

The initial conditions are

$$T_{h,c,cf}(s,0) = \text{constant(known temperature)} \quad \text{i.e., at } s = s \text{ and } t = 0. \tag{12c}$$

6. Non-dimensionalisation

Following non-dimensional parameters have been introduced for transforming the conservation equations in dimensionless form.

$$S = \frac{s}{L_1}; \quad K_1 = \frac{L_2}{L_1}; \quad K_2 = \frac{L_1}{D}, \tag{13a}$$

$$\tau = t\left[\left(\frac{\mu D}{\rho A_s}\right)_{cf} \frac{1}{L_1}\right], \tag{13b}$$

$$\theta_{h,c,cf} = \frac{(T_{h,c,cf} - T_{ci})}{(T_{hi} - T_{ci})}, \tag{13c}$$

$$C^*_{h,c,cf} = \frac{C_{h,c,cf}}{(\mu c D)_{cf}}, \tag{13d}$$

$$(UA)^*_{h,c} = \frac{(UA)_{h,c}}{(\mu c D)_{cf}}, \tag{13e}$$

$$Ntu^*_{h,c} = \frac{(UA)^*_{h,c}}{C^*_{h,c}}, \tag{13f}$$

$$Gr_L = \frac{\rho_{ci}^2 g \beta D^3 (T_{hi} - T_{ci})}{\mu_{cf}^2}, \tag{13g}$$

where ρ_{ci} is the reference density taken at the cold stream inlet temperature, i.e., T_{ci}.

$$R_{h,c} = \frac{(\rho A_s c)_{cf}}{(\rho A_s c)_{h,c}} \tag{13h}$$

ratio of coupling fluid heat capacitance to hot/cold stream heat capacitance per unit length.

Hence, the momentum equation (4) is expressed in dimensionless form as follows:

$$\frac{\partial P^*_t}{\partial S} = -\left[\frac{\partial C^*_{cf}}{\partial \tau} + \frac{\rho_{ci}^2 (A_s^2)_{cf} g L_1 \sin\phi}{\mu_{cf}^2 D^2} - \frac{\pi^2}{16} Gr_L K_2 \theta_{cf} \sin\phi + \frac{\pi^b a}{2^{2b-1}} K_2 C^{*2-b}_{cf}\right]. \tag{14}$$

The loop momentum equation (6) is non-dimensionalised and is given below.

$$\frac{\partial C^*_{cf}}{\partial \tau} + \frac{\pi^b a K_2}{2^{2b-1}} (C^*_{cf})^{2-b} + \frac{\pi^2}{2^5} Gr_L K_2 \frac{1}{(1+K_1)} \left[\int_{(K_1+2)}^{2(K_1+1)} \theta_{cf}\, dS - \int_1^{(K_1+1)} \theta_{cf}\, dS\right] = 0. \tag{15}$$

The energy equations given in (7)–(11) are recast in non-dimensional form as given in (16)–(20).

$$\frac{\partial \theta_h}{\partial \tau} - C^*_h R_h \frac{\partial \theta_h}{\partial S} + Ntu^*_h C^*_h R_h (\theta_h - \theta_{cf}) = 0, \tag{16}$$

$$\frac{\partial \theta_{cf}}{\partial \tau} + C^*_{cf} \frac{\partial \theta_{cf}}{\partial S} + Ntu^*_h C^*_h (\theta_{cf} - \theta_h) = 0, \tag{17}$$

$$\frac{\partial \theta_c}{\partial \tau} - C^*_c R_c \frac{\partial \theta_c}{\partial S} + Ntu^*_c C^*_c R_c (\theta_c - \theta_{cf}) = 0, \tag{18}$$

$$\frac{\partial \theta_{cf}}{\partial \tau} + C^*_{cf} \frac{\partial \theta_{cf}}{\partial S} + Ntu^*_c C^*_c (\theta_{cf} - \theta_c) = 0, \tag{19}$$

$$\frac{\partial \theta_{cf}}{\partial \tau} + C^*_{cf} \frac{\partial \theta_{cf}}{\partial S} = 0. \tag{20}$$

7. Solution

On integration, Eq. (14) yields the following equation for the total pressure drop difference.

$$\Delta P^*_t(S,\tau) = P^*_t(S,\tau) - P^*_t(0,\tau)$$
$$= -\left[\frac{\partial C^*_{cf}}{\partial \tau} S + P^*_S - \frac{\pi^2}{16} Gr_L K_2 \int_0^S \theta_{cf} \sin\phi \, dS + \frac{\pi^b a}{2^{2b-1}} K_2 C^{*2-b}_{cf} S\right]. \quad (21)$$

Now following the methodology suggested by Mertol et al. [9], the dynamic pressure difference can be obtained by integrating Eq. (14):

$$\Delta P^*_d(S,\tau) = P^*_d(S,\tau) - P^*_d(0,\tau)$$
$$= -\left[\frac{\partial C^*_{cf}}{\partial \tau} S - \frac{\pi^2}{16} Gr_L K_2 \int_0^S \theta_{cf} \sin\phi \, dS + \frac{\pi^b a}{2^{2b-1}} K_2 C^{*2-b}_{cf} S\right], \quad (22)$$

where

$$P^*_d = P^*_t - P^*_S \quad (23)$$

and

$$P^*_S = -\frac{\rho^2_{ci}(A^2_s)_{cf} g L_1}{\mu^2_{cf} D^2} \sin\phi S; \qquad P^*_t = \frac{P_t \rho_{ci}(A^2_s)_{cf}}{\mu^2_{cf} D^2}. \quad (24)$$

The non-dimensional boundary conditions become

$$\theta_h(S,\tau) = 1.0 \quad \text{at } S = 1.0, \quad (25a)$$

$$\theta_c(S,\tau) = 0.0 \quad \text{at } S = (K_1 + 2). \quad (25b)$$

The non-dimensional initial conditions become

$$\theta_{h,c,cf}(S,\tau) = 0.0 \quad \text{at } S = S \text{ and } \tau = 0. \quad (25c)$$

Distribution of dynamic pressure at steady state may be obtained by simultaneous solution of the above system of equations by setting the transient terms in them equal to zero.

$$\Delta P^*_{dss} = \begin{cases} -\frac{\pi^b a}{2^{2b-1}} K_2 (C^*_{cf})^{2-b} S, & 0 \leqslant S \leqslant 1, \quad (26a) \\ \frac{\pi^2}{2^4} Gr_L K_2 \theta_{cfss2}(S-1) - \frac{\pi^b a}{2^{2b-1}} K_2 (C^*_{cf})^{2-b} S, & 1 \leqslant S \leqslant (K_1+1), \quad (26b) \\ \frac{\pi^2}{2^4} Gr_L K_1 K_2 \theta_{cfss2} - \frac{\pi^b a}{2^{2b-1}} K_2 (C^*_{cf})^{2-b} S, & (K_1+1) \leqslant S \leqslant (K_1+2), \quad (26c) \\ \frac{\pi^2}{2^4} Gr_L K_1 K_2 \theta_{cfss2} - \frac{\pi^2}{16} Gr_L K_2 \theta_{cfss1}[S-(K_1+2)] - \frac{\pi^b a}{2^{2b-1}} K_2 (C^*_{cf})^{2-b} S, & (K_1+2) \leqslant S \leqslant 2(K_1+1). \quad (26d) \end{cases}$$

Eqs. (26a)–(26d) are the explicit functions. Therefore, it is obvious from these equations that the location of extrema are obtained at $S = 1$ and at $S = (K_1 + 1)$ and the same has been obtained from numerical solution, which has been described in the next section.

Steady state total pressure variation along the loop is similar to Eqs. (26a)–(26d) with the inclusion of static pressure, P^*_S, (function of space coordinate S and angle of inclination of loop sections) in each of the equations of (26a)–(26d). However, angle of inclination, ϕ, is zero for both top and bottom horizontal sections, therefore, the term P^*_S is zero for these sections. The steady state and transient variation of total pressure has also been studied and presented in the later sections. The numerical value, $\left(\frac{\rho^2_{ci}(A^2_s)_{cf} g L_1}{\mu^2_{cf} D^2}\right)$, in the static pressure term, P^*_S, has been taken as 2.0×10^8 for presenting the total pressure analysis.

Further, limiting analytical expressions have been derived for the steady state values of dynamic pressure, considering the following two cases.

Case I. When C^*_h and C^*_c tend to infinity, effectiveness of both hot and cold heat exchangers become 1.0. Further, $\theta_{cfss2} = 1.0$, $\theta_{cfss1} = 0.0$ and $C^*_{cf} = \left[N Gr_L \frac{K_1}{(1+K_1)}\right]^{\frac{1}{2-b}}$ [8]. Where $N = \frac{\pi^{2-b}}{2^{6-2b} a}$.

Therefore, it provides

$$\Delta P^*_{dss} = \begin{cases} -\frac{\pi^2}{2^5} \frac{K_1 K_2}{(1+K_1)} Gr_L S, & 0 \leqslant S \leqslant 1, \quad (27a) \\ \frac{\pi^2}{2^4} K_2 Gr_L \left[S\left(1 - \frac{K_1}{2(1+K_1)}\right) - 1\right], & 1 \leqslant S \leqslant (K_1+1), \quad (27b) \\ -\frac{\pi^2}{2^5} \frac{K_1 K_2}{(1+K_1)} Gr_L S, & (K_1+1) \leqslant S \leqslant (K_1+2), \quad (27c) \\ \frac{\pi^2}{2^4} K_1 K_2 Gr_L \left(1 - \frac{S}{2(1+K_1)}\right), & (K_1+2) \leqslant S \leqslant 2(K_1+1). \quad (27d) \end{cases}$$

Case II. When $C^*_h = C^*_c = C^*, C^* \geqslant C^*_{cf}$ and $Ntu^*_h = Ntu^*_c = Ntu^*$, then $\varepsilon^*_h = \varepsilon^*_c = \varepsilon$. Where ε is the effectiveness, $\frac{1 - e^{-Ntu^*\left(1 - \frac{C^*_{cf}}{C^*}\right)}}{1 - \frac{C^*_{cf}}{C^*} e^{-Ntu^*\left(1 - \frac{C^*_{cf}}{C^*}\right)}}$.

Therefore, the steady state non-dimensional riser, downcomer temperatures and coupling fluid flow rate become

$$\theta_{cfss2} = \frac{1}{2 - \varepsilon}, \quad (28)$$

$$\theta_{cfss1} = \left(1 - \frac{1}{2 - \varepsilon}\right), \quad (29)$$

$$C^*_{cf} = \left[N Gr_L \frac{K_1}{(1+K_1)} \frac{\varepsilon}{(2-\varepsilon)}\right]^{\frac{1}{(2-b)}}. \quad (30)$$

And the dynamic pressure distribution under steady state can be obtained as

$$\Delta P^*_{\mathrm{dss}} = \begin{cases} -\frac{\pi^2}{2^5}\frac{K_1K_2}{(1+K_1)}Gr_{\mathrm{L}}\frac{\varepsilon}{(2-\varepsilon)}S, \quad 0 \leqslant S \leqslant 1, & (31a)\\ \frac{\pi^2}{2^4}K_2Gr_{\mathrm{L}}\frac{1}{(2-\varepsilon)}(S-1) \\ \quad -\frac{\pi^2}{2^5}\frac{K_1K_2}{(1+K_1)}Gr_{\mathrm{L}}\frac{\varepsilon}{(2-\varepsilon)}S, \\ \quad 1 \leqslant S \leqslant (K_1+1), & (31b)\\ \frac{\pi^2}{2^4}K_1K_2Gr_{\mathrm{L}}\frac{1}{(2-\varepsilon)} \\ \quad -\frac{\pi^2}{2^5}\frac{K_1K_2}{(1+K_1)}Gr_{\mathrm{L}}\frac{\varepsilon}{(2-\varepsilon)}S, \\ \quad (K_1+1) \leqslant S \leqslant (K_1+2), & (31c)\\ \frac{\pi^2}{2^4}K_2Gr_{\mathrm{L}}\left(\frac{K_1}{(2-\varepsilon)}-\left(1-\frac{1}{(2-\varepsilon)}\right)S\right) \\ \quad -\frac{\pi^2}{2^5}\frac{K_1K_2}{(1+K_1)}Gr_{\mathrm{L}}\frac{\varepsilon}{(2-\varepsilon)}S, \\ \quad (K_1+2) \leqslant S \leqslant 2(K_1+1). & (31d) \end{cases}$$

8. Results and discussion

The developments of circulation rate, temperature field and local pressure in a NCL are closely related and cannot be studied in isolation. In the present section, the pressure variation under both steady and transient state has been described in connection with the change in circulation rate and local temperature.

It may be noted that the conservation equations for the transient state cannot be solved analytically. Eqs. (15)–(20) have been solved using a Finite Element formulation. The simulation starts from a cold state. The coupling fluid and the two external fluid streams are at isothermal condition, at a temperature equal to that of the cold stream at the entry to the CEHE. Then a step input is given to the hot fluid inlet temperature. The simulation is continued till a new steady state is achieved. The circulation rate reaches its new steady state value from a low initial value. For most of the combinations of operating parameters, the flow goes to the turbulent regime from the laminar one. The program discriminates between the two regimes taking a value of critical Reynolds number as 2000. In the friction factor correlation, values of '*a*' are taken as 16 and 0.079 for laminar and turbulent flows, respectively and values for '*b*' are taken 1.0 and 0.25 for the corresponding cases. No transition zone has been considered in the present work.

Inception of fluid flow in the loop is associated with the instabilities present in the system [13]. Modelling of such instabilities are beyond the scope of the present analysis. Therefore, to initialize the simulation a small unidirectional flow in the counter-clockwise direction has been imposed. The Finite Element program uses an iterative scheme. The flow rate of the coupling fluid is assumed (a small unidirectional flow) and it is corrected till the loop momentum equation is satisfied. To start with, the loop temperature field is determined by solving Eqs. (16)–(20), with an initially assumed coupling fluid flow rate, using two boundary conditions as mentioned in Eqs. (25a) and (25b). With this temperature field the flow rate is obtained by solving Eq. (15). As the energy and loop momentum equations are coupled in nature, at the beginning of the first time step a small non-dimensional temperature (arbitrarily small positive value) has been assigned for the coupling fluid at the downcomer end (beginning of HEHE, M). This demands use of two error criteria, one for the coupling fluid velocity and the second for the temperature. Eqs. (21) and (22) are evaluated for total and dynamic pressures, respectively once the two prescribed error criteria are satisfied. The integrals in Eqs. (15), (21) and (22) have been evaluated by Gauss–Legendre quadrature. Further details of the solution procedure may be obtained from Rao [8].

In Figs. 2 and 4 the variation of temperature and dynamic pressure over the entire loop have been given under the steady state for different values of the heat capacity rates of the external fluid streams and for the following geometrical and physical parameters; $Ntu^*_{\mathrm{h}} = 5.0$, $Ntu^*_{\mathrm{c}} = 2.0$, $Gr_{\mathrm{L}} = 1.0\times10^7$, $R_{\mathrm{h}} = 5.0\times10^3$, $R_{\mathrm{c}} = 1.0\times10^3$, $K_1 = 2.0$ and $K_2 = 20.0$. The corresponding change of the circulation rate is depicted in Fig. 3.

As the heat capacity rate of the external fluid streams increases there is an increase in the riser temperature and decrease in the downcomer temperature (Fig. 2) due to the improvement in heat exchange between the coupling fluid and the external fluid streams. This in turn increases the flow rate (C^*_{cf}) as can be seen from Fig. 3. Further, it can be seen from Fig. 4 that as the flow rate increases with the increase of C^*_{h} and C^*_{c}, pressure drop increases in the HEHE section due to viscous losses. Dynamic pressure difference increases along the riser and reaches its maximum value in the loop at the end of the riser section. This is due to the rise in total pressure from the contribution of buoyancy. There onwards the

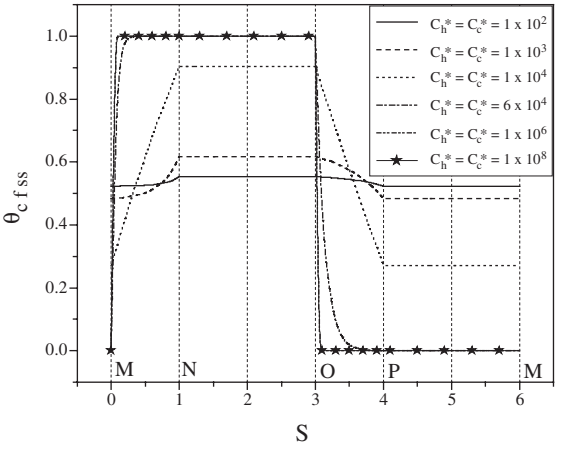

Fig. 2. Steady state loop temperature distribution.

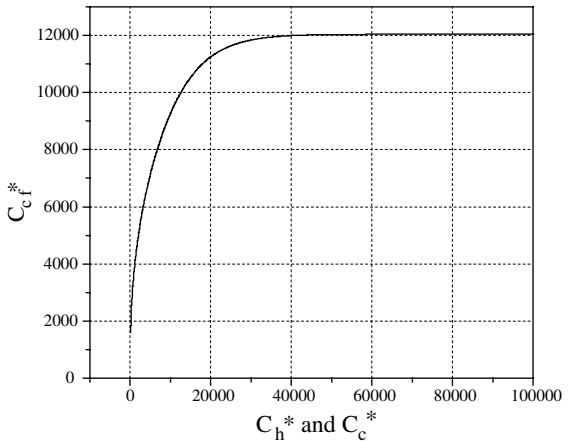

Fig. 3. Steady state coupling fluid flow rate.

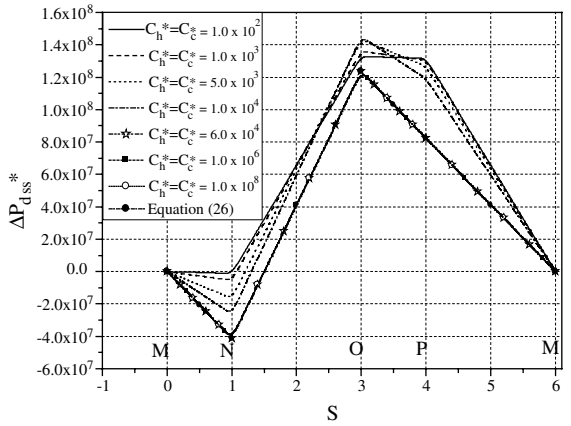

Fig. 4. Steady state dynamic pressure distribution.

dynamic pressure difference decreases in the remaining part of the loop (CEHE and downcomer).

From Eqs. (25a) and (25b) one gets the maximum limit for riser temperature as 1.0 and the minimum value of the downcomer temperature as 0.0. This is possible when both C_h^* and C_c^* tend to infinity as mentioned in the special case I. Numerically, θ_{cfss2} and θ_{cfss1} approaches their upper and lower limits respectively, for high values of C_h^* and C_c^* i.e., $C_h^* = C_c^* = 6 \times 10^4$ (Fig. 2). In this case there is a maximum loop temperature difference (1.0–0.0 = 1.0), which in turn gives the maximum density difference makes the fluid to flow at the highest possible rate. As a result, pressure drop is maximum in HEHE and the pressure rise is lower along the riser (Fig. 3) as there is a substantial increase in frictional pressure drop due to the increase in circulation rate. This further results into decrease of pressure in both CEHE and downcomer and makes the value of dynamic pressure always lower than those obtained at other values of C_h^* and C_c^*.

The curves for dynamic pressure difference at various values of heat capacity rates share a few common features. The slopes of the pressure difference curve for HEHE and CEHE are identical in magnitude and sign. The slope of the curve in the riser section is more than that of the curve in the downcomer section. This is obvious as the positive pressure head generated in the riser balances the frictional pressure drop in the entire loop. Interestingly, it can be noted that there is no change of slope between CEHE and downcomer for the limiting condition of infinite heat capacity rate of the external fluids ($C_h^* = C_c^* > 6 \times 10^4$). As the flow rate is maximum at this condition the frictional pressure drop is much higher than the gravitational pressure head. Therefore, though the CEHE and the downcomer are at different orientations with respect to gravity, the difference of slope of the pressure difference curve for these two sections is negligible. For the presentation of results, curves are plotted taking identical values of the heat capacity rate for both the heat exchangers. The nature of the curves does not change if different heat capacity rates are considered for the heat exchangers.

One can see that, for the estimation of dynamic pressure, the static pressure, P_S^*, has been subtracted from the total pressure, P_t^* (Eq. (23)). The pressure, P_S^*, is the hydrostatic pressure only when the temperature in the loop is *everywhere* equal to the inlet temperature (non-dimensional) of the cold stream i.e., at initial condition (zeroth time). Therefore, the pressure P_d^* is a reasonable approximation to the dynamic pressure [9]. From Eq. (22) one can see that under steady state conditions ($\frac{\partial C_{cf}^*}{\partial \tau} = 0$) the change in dynamic pressure is balanced by buoyancy and friction. The datum for the pressure has been taken to be the value at $S = 0$ (Eq. (22)). Friction always opposes the flow, contribution to a negative pressure gradient, while buoyancy acts to assist the flow at some locations and oppose the flow in others. Hence, the pressure gradient is positive when buoyancy assists the flow strongly enough to overcome the friction.

Fig. 5a and b show the total pressure variation at the steady state for two different numerical values of P_S^*, $\left(\frac{\rho_{ci}^2 (A_s^2)_{cf} g L_1}{\mu_{cf}^2 D^2}\right)$. As it has been demonstrated in later sections that for a reasonable physical and geometrical values, static pressure nullifies the significance of presence of dynamic pressure at any cross section of the loop. This has been illustrated in Fig. 5b for taking a numerical value of $P_S^* = 2 \times 10^{10}$ at which variation of hot and cold stream heat capacity rates is having no effect on total spatial pressure variation. The numerical value $P_S^* = 2 \times 10^{10}$ is obtained for the values of ρ_{ci}, μ_{cf}, L_1 and D as 998.0 kg/m^3, 959.0×10^{-6} kg/m s, 1.0 m and 0.0508 m, respectively. On the other hand, the numerical

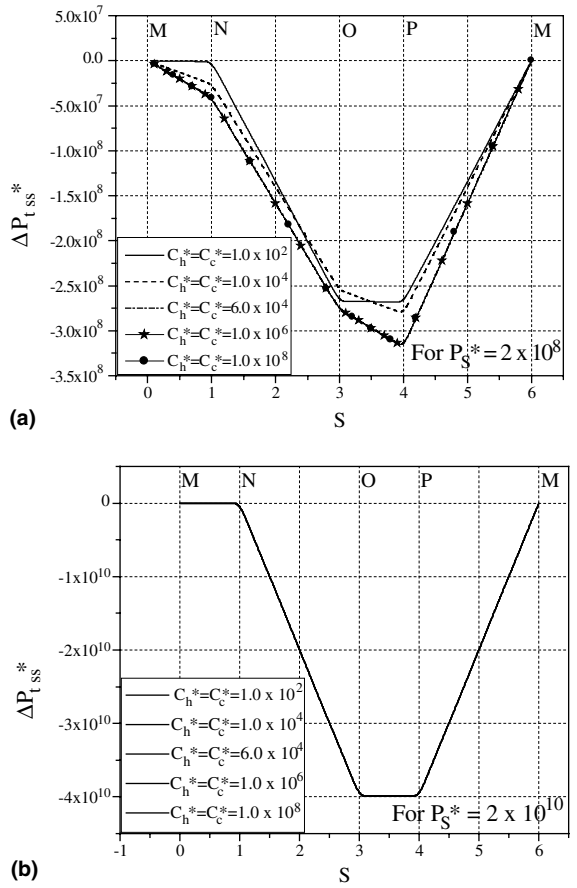

Fig. 5. Steady state total pressure distribution: (a) for a numerical value of $P_S^* = (2 \times 10^8)$, (b) for a numerical value of $P_S^* = (2 \times 10^{10})$.

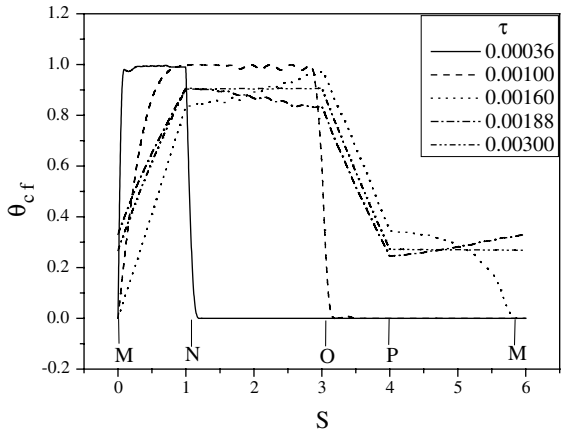

Fig. 6. Temporal development of temperature profile.

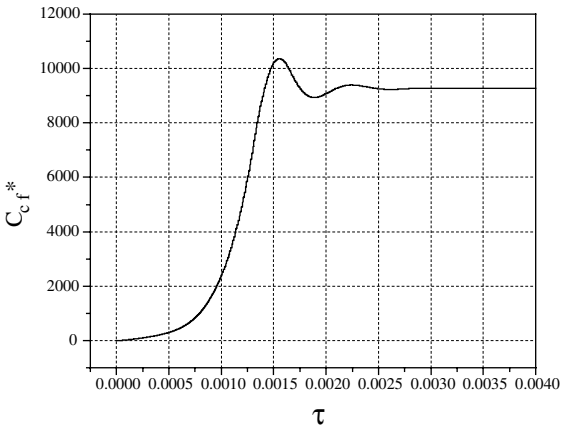

Fig. 7. Temporal development of flow field.

value of $P_S^* = 2 \times 10^8$ (which has been taken arbitrarily to show the effect of dynamic and static pressure variation together) shows the spatial variation of total pressure with the variation of hot and cold stream heat capacity rates (Fig. 5a). The geometrical and physical parameters have been used for total pressure variation are similar to that of dynamic pressure variation. It is well known that the static pressure decreases in upward movement (riser) and increases in downward movement (downcomer) and variation of static pressure in bottom and horizontal zones is zero. The Fig. 5a shows the similar trend in which, the pressure variation is of only dynamic pressure along the heating and cooling zones and is combination of static and dynamic pressures along the riser and downcomer.

The transient variation of the temperature field and the circulation rate are depicted in Figs. 6 and 7 for a typical case. Here, the geometrical and physical parameters are identical to those, which are taken for the previous analysis. However, the C_h^* and C_c^* are 1.0×10^4 and 1.0×10^4, respectively. Some of the loop parameters (Ntu_h^* and Ntu_c^*) and geometrical parameters (K_1 and K_2) have been selected arbitrarily without keeping any specific application in mind. However, the results obtained thereby helps to understand the general behaviour of the NCL. A numerical value of 2×10^8 for P_S^* has been taken in evaluating the total pressure. The corresponding dynamic and total pressure variations are given in Figs. 8 and 9.

It can be seen from Fig. 7 that the system reaches the steady state through some oscillations for a finite step perturbation of the hot fluid inlet temperature. While the continuous variation of the circulation rate from the inception of the perturbation up to the steady state has been depicted, the pressure and temperature variations over the loop have been presented for different time steps. The time step values have been selected carefully to demonstrate the phenomenological developments during the transient period.

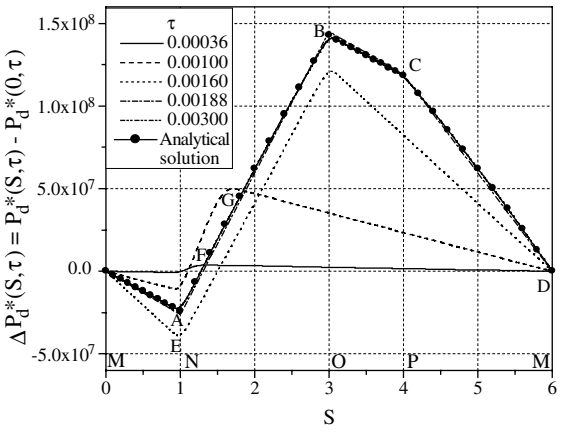

Fig. 8. Transient dynamic pressure variation along the loop.

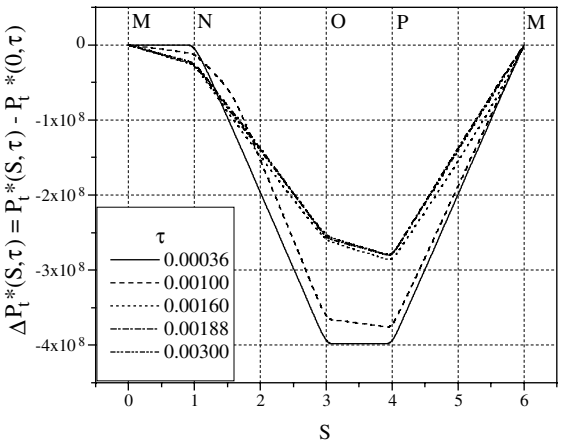

Fig. 9. Transient total pressure variation along the loop.

Just after the imposition of the finite perturbation ($\tau = 0.00036$) the flow is negligibly small (Fig. 7). Further, at this stage there is a rise in temperature of the coupling fluid only in the HEHE. At the remaining sections of the loop except very close to the entry of the riser the coupling fluid temperature remains at its initial low value (Fig. 6). For the corresponding condition in Fig. 8, there is a small pressure drop in HEHE, a relatively larger pressure rise in a very small section of the riser close to its entry, and then a continuous fall in pressure in CEHE and in the downcomer. With the passage of time, the heating effect of the HEHE penetrates to a larger distance into the riser as can be seen from the temperature traces in Fig. 6. As this gives rise to a higher driving force due to gravity, the flow rate also increases. This situation is depicted in Fig. 8 for $\tau = 0.001$. From the uprising portion of the pressure difference curve one can approximately determine the progress of the heated fluid front in the riser at this time. At $\tau = 0.0016$ a unique situation may be observed. At this juncture of time, due to initial oscillations, the flow rate of the coupling fluid is maximum – even more than its steady state value. This gives maximum value of pressure difference across any section of the loop. Finally, the pressure difference have been depicted for $\tau = 0.003$ where the new steady state has already been reached. The pressure difference curve also matches exactly with the analytical results obtained for the steady state. All the pressure difference curves depicted in Figs. 4 and 8 starts from a zero value at $S = 0$ (the selected datum level for the pressure calculation) and terminates with the same value at $S = 6$. This indicates a balance between the buoyancy force and the viscous dissipation irrespective of the operating parameters and steady or transient state.

At the beginning of imposition of finite perturbation (0.00036) the flow is negligibly small, therefore, the static pressure variation completely dominates the dynamic pressure variation as illustrated in Fig. 9. With the increase of flow rate the dominance of static pressure gradually diminishes and the pressure variation becomes the combination of both dynamic and static till the system reaches the steady state (Fig. 9). The numerical value of P_S^* has been taken as $2\times\ 10^8$ along with the identical operating and geometrical parameters as it has been considered in the temporal variation of dynamic pressure.

Though the variation of dynamic pressure is of interest, the ratio of the maximum dynamic pressure to maximum hydrostatic pressure is of great significance. Therefore, the ratio of maximum dynamic pressure variation at the exit of the riser to maximum hydrostatic pressure has been considered for this study. This ratio can be written as follows:

$$\frac{(\Delta P^*_{\mathrm{dss\,max}})}{(\Delta P^*_{\mathrm{S}})} = \frac{\frac{\pi^2}{16} Gr_{\mathrm{L}} \theta_{\mathrm{cfss2}} K_1}{\frac{\rho_{\mathrm{ci}}^2 (A_{\mathrm{s}}^2)_{\mathrm{cf}} g L_1}{\mu_{\mathrm{cf}}^2 D^2}} - \frac{\frac{\pi^b a}{2^{2b-1}} K_2 (K_1+1)(C^*_{\mathrm{cfss}})^{2-b}}{\frac{\rho_{\mathrm{ci}}^2 (A_{\mathrm{s}}^2)_{\mathrm{cf}} g L_1}{\mu_{\mathrm{cf}}^2 D^2}}. \tag{32}$$

The above equation can further be simplified as

$$\frac{(\Delta P^*_{\mathrm{dss\,max}})}{(\Delta P^*_{\mathrm{S}})} = [\beta (T_{\mathrm{cfss2}} - T_{\mathrm{ci}})] - \left(\frac{2^{5-2b} a}{\pi^{2-b}} \frac{\mu_{\mathrm{cf}}}{\rho_{\mathrm{ci}}^2} \frac{(1+K_1)}{D^4 c_{\mathrm{cf}}} C_{\mathrm{cfss}} \right). \tag{33}$$

The simplified dimensional loop momentum equation can be written as follows.

$$C_{\mathrm{cfss}}^{2-b} = \frac{\pi^{2-b}}{2^{6-2b}} \frac{\rho_{\mathrm{ci}}^2 g \beta D^{5-b} c_{\mathrm{cf}}^{2-b}}{\mu_{\mathrm{cf}}^b} \frac{K_1}{(1+K_1)} (T_{\mathrm{cfss2}} - T_{\mathrm{cfss1}}) \tag{34}$$

and the steady state riser and downcomer temperatures (dimensional) may be written as

$$T_{\mathrm{cfss2}} = \left[T_{\mathrm{cfss1}} - \frac{C_{\mathrm{min,h}}}{C_{\mathrm{cfss}}} \varepsilon_{\mathrm{h}} (T_{\mathrm{hi}} - T_{\mathrm{cfss1}}) \right], \tag{35}$$

$$T_{\mathrm{cfss1}} = \left[T_{\mathrm{cfss2}} - \frac{C_{\mathrm{min,c}}}{C_{\mathrm{cfss}}} \varepsilon_{\mathrm{c}} (T_{\mathrm{ci}} - T_{\mathrm{cfss2}}) \right], \tag{36}$$

where

$$\varepsilon_{\mathrm{h,c}} = \frac{1 - \mathrm{e}^{-Ntu_{\mathrm{h,c}}\left(1 - \frac{C_{\mathrm{min,h,c}}}{C_{\mathrm{max,h,c}}}\right)}}{1 - \frac{C_{\mathrm{min,h,c}}}{C_{\mathrm{max,h,c}}} \mathrm{e}^{-Ntu_{\mathrm{h,c}}\left(1 - \frac{C_{\mathrm{min,h,c}}}{C_{\mathrm{max,h,c}}}\right)}}. \tag{37}$$

To determine the C_{cfss}, T_{cfss2} and T_{cfss1}, the coupled Eqs. (34)–(36) have been solved iteratively. The detailed computational procedure has been given in Rao [8]. Here, the coupling fluid has been assumed as water. The physical properties, at 22 °C, ρ_{cf}, μ_{cf}, c_{cf} and β have been taken as 998.0 kg/m^3, 959.0×10^{-6} kg/m s, 4.181 kJ/kg K and 227.5×10^{-6} K^{-1}, respectively [14]. The hot and cold stream heat capacity rates have been varied from 0.05 to 50 kW/K. The hot stream inlet temperature has been varied from 100 to 200 °C and cold stream temperature has been kept constant, 20 °C. Ntu_{h} and Ntu_{c} values have also been varied from 2 to 5. The geometrical dimensions such as diameters, 0.0508 and 0.1016 m for the heat exchanger, and height to horizontal length ratio of 2–4 for the loop have been considered. With the various combinations of above values the minimum and maximum values of $\frac{(\Delta P^*_{\mathrm{dss\,max}})}{(\Delta P^*_{\mathrm{S}})}$ have been determined and found as 0.04 and 0.2, respectively. Thus, the static pressure is 25–5 times greater than the dynamic pressure. Therefore, the total pressure is essentially the hydrostatic pressure. This is in well conformity with the study of Mertol et al. [9] who have observed in their analysis that the static pressure is up to four orders of magnitude greater than the dynamic pressure.

9. Conclusion

The present study deals with the variation of dynamic and total pressure in a rectangular NCL of uniform circular cross section with end heat exchangers. The generalised momentum and energy equations have been derived for the transient operating condition in a one dimensional frame. A Finite Element Technique has been used to solve the set of seven coupled deferential and integral equations in an iterative manner. Temporal dynamic pressure distribution has been presented along with the temporal variation in temperature distribution and development of flow rate. Additionally, pressure distribution equations for the steady state have been derived analytically. Two special cases have been considered and limiting analytical expressions for them have been deduced. Further, spatial steady state total pressure variation as well as temporal total pressure variations have also been presented. The ratio of maximum dynamic pressure to maximum static pressure has been computed taking realistic values for operating parameters, physical properties and geometrical dimensions. It has been found that the total pressure is essentially a static pressure.

References

[1] Y. Zvirin, A review of natural circulation loops in pressurized water reactors and other systems, Nucl. Eng. Design 67 (1981) 203–225.
[2] A. Mertol, R. Greif, in: S. Kakac, W. Aung, R. Viskanta (Eds.), A Review of Natural Circulation Loops, Natural Convection: Fundamentals and Applications, Hemisphere, New York, 1985, pp. 1033–1071.
[3] R. Greif, Natural circulation loops, ASME J. Heat Transfer 110 (1988) 1243–1258.
[4] P.K. Vijayan, S.K. Mehta, A.W. Date, On the steady-state performance of natural circulation loops, Int. J. Heat Mass Transfer 34 (1991) 2219–2230.
[5] P.K. Vijayan, H. Austregesilo, Scaling law for single-phase natural circulation loops, Nucl. Eng. Design 152 (1994) 331–347.
[6] A. Pacheco-Vega, W. Franco, H.C. Cheng, M. Sen, Nonlinear analysis of tilted toroidal thermosyphon models, Int. J. Heat Mass Transfer 45 (2002) 1379–1391.
[7] N.M. Rao, M. Mishra, B. Maiti, P.K. Das, Effect of end heat exchanger parameters on the performance of a natural circulation loop, Int. Comm. Heat Mass Transfer 29 (2002) 509–518.
[8] N.M. Rao, Investigations on buoyancy induced circulation loops, Ph.D., Thesis, Indian Institute of Technology, Kharagpur, 2002.
[9] A. Mertol, A. Lavine, R. Greif, A study of the variation of the pressure in a natural circulation loop, Int. J. Heat Mass Transfer 27 (1984) 626–630.
[10] R. Greif, Y. Zvirin, A. Metrol, The transient and stability behavior of a natural convection loop, ASME J. Heat Transfer 101 (1979) 684–688.
[11] Y. Zvirin, R. Greif, Transient behaviour of natural circulation loops: two vertical branches with point heat source and sink, Int. J. Heat Mass Transfer 22 (1979) 499–504.
[12] A. Mertol, R. Greif, Y. Zvirin, The transient, steady state and stability behavior of a thermosyphon with through-flow, Int. J. Heat Mass Transfer 24 (1981) 621–633.
[13] H.F. Creveling, J.F. De Paz, J.Y. Baladi, R.J. Schoenhals, Stability characteristics of a single phase free convection loop, J. Fluid Mech. 67 (Part1) (1975) 65–84.
[14] F.P. Incropera, D.P. DeWitt, Fundamentals of Heat and Mass Transfer, John Wiley and Sons, Singapore, 1996.